Dalitz plots as a tool to resolve nonsequential paths in strong-field triple ionization

Hui Jiang,[1] Dmitry Efimov,[2] Feng He,[1,3,*] and Jakub S. Prauzner-Bechcicki[4]

[1]*Key Laboratory for Laser Plasmas (Ministry of Education) and School of Physics and Astronomy, Collaborative Innovation Center for IFSA, Shanghai Jiao Tong University, Shanghai 200240, China*

[2]*Department of Theoretical Physics, Faculty of Fundamental Problems of Technology, Wrocław University of Science and Technology, 50-370 Wrocław, Poland*

[3]*CAS Center for Excellence in Ultra-intense Laser Science, Shanghai 201800, China*

[4]*Instytut Fizyki imienia Mariana Smoluchowskiego, Uniwersytet Jagielloński, Łojasiewicza 11, 30-348 Kraków, Poland*

(Received 22 February 2022; accepted 10 May 2022; published 23 May 2022)

Strong-field triple ionization of atoms is studied by performing classical-trajectory Monte Carlo simulations. The momentum distributions of three electrons are visualized via Dalitz plots, exhibiting clear electronic correlations. Separated traces of various nonsequential paths are identified in these ternary spectra, including channels with multiple recollisions. It is proposed that Dalitz plots can be used as a valuable tool to study correlated electron dynamics in strong fields, in particular, as a method to retrieve from experimental data relative roles of various channels of nonsequential ionization such as direct ionization, recollision-induced excitation with subsequent ionization, or a multirecollison.

DOI: 10.1103/PhysRevA.105.053119

I. INTRODUCTION

Correlation dynamics between electrons in atomic ionization has been studied for a long time and still remains a hot topic due to the rich physical images [1]. Nowadays, it is possible to study the one-electron dynamics on the attosecond timescale employing the concept of streaking spectroscopy [2,3]. However, direct observation of multielectron dynamics has so far been extremely difficult. When it comes to the correlations between electrons that lead to multiple ionization under a strong laser field, the famous knee structure in the intensity-dependent ion yields [4,5] has been widely studied, which indicates a nonsequential regime in which collisions between electrons play a key role. For strong-field nonsequential multiple ionization, because the final drift momenta of the electrons can be approximated by the vector potential at the ionization time, we can deduce the possible ionization mechanisms induced by different correlation effects in which the emission time of electrons may be different. Thus, to study the details of correlation dynamics induced by recollisions, the correlated momentum spectrum of two electrons has been widely used for nonsequential double ionization (NSDI) with the help of cold-target recoil-ion momentum spectroscopy [6]. It turned out that specific structures in correlated electron momentum spectra reveal different dynamics. The fingerlike pattern showed an asymmetric electron energy sharing after the recollision [7,8], a cross-shaped structure pointed out the role of recollision-induced excitation with subsequent ionization (RESI) [9], the unusual spectra of the high-Z atom (Xe) shed light on the shielding effect in NSDI [10], and the anticorrelated two-electron emission can be caused by a slingshot mechanism [11]. The correlated momentum spectrum can provide much more information as compared to the nuclear momentum distribution. However, when it comes to nonsequential triple ionization (NSTI), only a few works [12,13] focused on the three-electron correlated momenta because of the severe difficulties in both experiments and theories.

Since there are three electrons involved in NSTI, various paths leading to the formation of the triple ion can be expected. Understanding the role of these different paths in strong-field dynamics is crucial for creating consistent theoretical models for complex atoms and molecules capable of describing their behavior in intense short laser fields. While the existing analytic and semianalytic models [1,14] include two active electrons at most, there is evidence that a number of phenomena, like creation and evolution of holes during strong-field dynamics [15,16], can only be explained with approaches including three or more active electrons. The three-active-electron models may serve as building blocks for a more precise description of complex systems under typical laser intensities for which nonsequential processes dominate [17].

The available experimental data related to triple atomic ionization include the ion momentum distributions and the electron energy distribution for a set of different target atoms, laser wavelengths, and laser intensities [18–22]. However, the predictions based on these data are limited because the electronic correlation information is not fully represented in it. For example, in Ref. [20] the authors deduced a possible NSTI mechanism such as sequential production of Ar^{2+} followed by NSDI, though the characteristics of the various possible NSTI channels are difficult to extract solely based on the ion momentum distributions. Thus, a new technique is needed to infer the various multiple ionization channels to understand the correlation effects induced by the rescattering.

*fhe@sjtu.edu.cn

Fortunately, the three-electron coincidence experiments providing correlated electronic distributions may be feasible in the future [18,23,24]. A natural question therefore arises as to whether it is possible to extract the details of the complex NSTI channels by analyzing the spectra of the three electrons' correlated momenta.

Yet even for the theorist it is not an easy task to get channel-resolved information on strong-field ionization. First, a very powerful tool used in strong-field physics is an analytical approach known as strong-field approximation, but it becomes very convoluted already for two electrons [25]. So it remains to use numerical methods. However, due to the involvement of three active electrons, it is extremely difficult to perform full-dimensional quantum-mechanical simulations for nonsequential triple ionization. There are mainly three approaches to treat atomic triple-ionization problems and it is instructive to briefly review their capabilities. The first one is the time-dependent close-coupling method [26,27]. It is a fully quantum-mechanical approach while it can only solve few-photon ionization problems. The tunneling dynamics is hard to incorporate in this approach; thus it has limited applicability for simulating femtosecond processes. Another approach is direct integration of the time-dependent Schrödinger equation (TDSE) with reduced dimensionality [17,28–33], which appears to be the most successful quantum model for studying particular ionization channels. Within this approach, one can define different channels according to the probability fluxes flowing between different regions on the grid, assigned to neutral atoms and single, double, and triple ions, respectively. This approach is good for gaining insight into the intrinsic dynamics of ionization, but it may never be possible to provide analogous procedures in actual experiments. Therefore, a direct simulation-experiment comparison is not possible for this approach and the results obtained are only qualitative and indicative. Although the experimental data reflect projections of the final electronic and ionic states, it is not yet clear how information about the different ionization channels can be extracted from the final wave function obtained by the TDSE solution. Thus, even though in Ref. [12] the authors succeeded to simulate the final electronic state and express it as the correlated momenta in a ternary spectrum (the so-called Dalitz plots) [34], the signs of particular different channels in those spectra remained unidentified. The third approach is the classical-trajectory Monte Carlo (CTMC) simulation, a method allowing one to obtain channel-resolved results, including electron momentum distributions. Each generated trajectory can be unambiguously attributed to an ionization path and to a point in momentum spectrum at the same time. The application of the CTMC simulation to study three-electron momentum spectra would solve the problem of establishing the channel-momentum spectrum correspondence within the standard limitations of the CTMC method (like the inability to correctly take into account electronic spin configurations and resonance transitions) as it has been successfully used for the simulation of two-electron correlated momentum spectra [8]. Yet the classical works [35–42] employing this method for triple ionization (TI) are rather focused on properties of ion momentum distributions in which three-electron correlation information is not fully represented and some of its features may be lost, for example, the asymmetrical energy sharing in the direct $(e, 3e)$ NSTI which would resemble the mechanisms behind the fingerlike pattern in NSDI. However, different channels may be mixed to obtain the same ion momentum distribution, making one lose track of them in the analyzed data. The classical-trajectory studies of three-electron momentum distributions are known [43], but they are not focused on differentiating ionization paths.

In this paper we set our goal to juxtapose information on NSTI channels and the final electronic momentum to reveal existing connections between them. The CTMC simulation can grasp the main picture of the rescattering scenario, and it has been demonstrated that it can quantitatively simulate the correlated momentum spectra. To this end, we perform semiclassical CTMC simulations [41] and study NSTI in Ar and Ne atoms. We generate the three-electron correlated momentum distributions that are mapped into ternary spectra. We find that different NSTI channels as well as their relative proportions can be extracted directly through analysis of such a spectrum. Furthermore, based on electron-resolved ternary spectra, we show that in this way the dynamics underlying the triple ionization can be investigated in more detail than by means of the ion momentum distributions solely. The obtained result allows us to unravel the information hidden in the ternary momentum spectra and will be very useful for interpretation of experimental data.

The paper is organized as follows. In Sec. II we describe our numerical model as well as the data representations we use further. Section III introduces the results of numerical simulations and then provides a discussion and analysis. The paper ends with a summary in Sec. IV. Atomic units are used throughout the paper unless specified otherwise.

II. NUMERICAL METHOD

We run the classical-trajectory Monte Carlo simulations [41] for the triple ionization of Ne and Ar atoms. The laser parameters we use are in the tunneling region for single ionization. In simulations, the first electron tunnels out, which is described by the Ammosov-Delone-Krainov theory [44]. The tunneling rate is formulated as

$$W_0(t) = 4\left(\frac{4I_{p1}}{|E(t)|}\right)^{2/\sqrt{2I_{p1}}-1} \exp\left(\frac{-2(2I_{p1})^{3/2}}{3|E(t)|}\right), \qquad (1)$$

with $E(t)$ the laser electric field. In this paper the laser pulse is polarized along the x axis and is expressed as $\mathbf{E}(t) = f(t)E_0 \sin(\omega t)\hat{\mathbf{x}}$, where $f(t)$ denotes an envelope starting with a plateau comprising several optical cycles (depend on the pulse duration) followed by the falling edge having two cycles. Here I_{p1} is the first-ionization potential for the atoms (0.579 a.u. for Ar and 0.793 a.u. for Ne). The initial position of the tunneling electron e_3 is determined by $\mathbf{x}_{3,0} = -\frac{I_{p1}}{|E(t)|}\hat{\mathbf{x}}$ and the transverse momentum is approximated by a Gaussian distribution with the width $\sqrt{\frac{|E(t)|}{2\sqrt{2I_{p1}}}}$. The nonadiabatic effect is neglected and thus the longitudinal momentum of the tunneling electron is zero. The initial conditions of the two bound electrons are constructed by minimizing the

two-electron Hamiltonian [41]

$$H_1 = \sum_{i=1}^{2}\left[\frac{1}{2}p_i^2 - \frac{3}{r_i} + V_H(r_i, p_i)\right] + \frac{1}{|\mathbf{r}_1 - \mathbf{r}_2|}, \quad (2)$$

where $V_H(r_i, p_i)$ is the Heisenberg core potential [45,46]

$$V_H(r_i, p_i) = \frac{(\xi_H \hbar)^2}{4\alpha r_i^2 m_e} \exp\left\{\alpha\left[1 - \left(\frac{r_i p_i}{\xi_H \hbar}\right)^4\right]\right\}. \quad (3)$$

We set $\alpha = 4$ and the value of ξ_H is determined by the ionization potential for different atoms (1.6352 for Ar and 1.3233 for Ne) [41,47]. The Heisenberg core potential is advantageous in constructing a stable two-bound-electron system and performs well when dealing with the collision dynamics [48,49]. Here we ignore the shift in energy level of bound electrons due to the IR field as in previous CTMC models [8,48]. The level shift of the ion comes from the Stark shift [50]. This is a linear Stark effect and the shift value is proportional to the dipole moment and the electronic field. When the electron states are degenerate, the Stark state counts and shows the polarization effects with a nonzero dipole moment. However, such a shift is always very small as the field is not strong enough. Thus, it is reasonable for us to ignore the level shift. When it comes to the shell effect of the atom, although it should be noted that when we deal with high-Z atoms (like Xe), the shell effect may be important and we had better use the modified screen potential [10]. In this work, because of our choice to study Ne and Ar, we do not need to take extra care about the shell effect when we construct the CTMC model. The neglect of the shell effect can also give us quantitative results compared with the experiments when we study Ne and Ar [36–39,41,48].

The tunneling events are uniformly sampled in the time region $[0, T]$ with the weight governed by $W_0(t)$. After the initial ensemble is set, we solve the canonical equations

$$\frac{d\mathbf{r}_i}{dt} = \frac{\partial H}{\partial \mathbf{p}_i}, \quad (4)$$

$$\frac{d\mathbf{p}_i}{dt} = -\frac{\partial H}{\partial \mathbf{r}_i}, \quad (5)$$

with the full Hamiltonian describing the interaction among three active electrons and the nucleus

$$H = \sum_{i=1}^{3}\left[\frac{1}{2}p_i^2 - \frac{3}{r_i} + V_H(r_i, p_i)\right] + \sum_{i,j=1;i<j}^{3}\frac{1}{|\mathbf{r}_i - \mathbf{r}_j|} + \sum_{i=1}^{3}\mathbf{r}_i \cdot \mathbf{E}(t). \quad (6)$$

We define different NSTI channels based on the number of recollisions and the number of emitted electrons within the time window T_c after the recollision [41]. In this work, to separate the direct ionization from the RESI mechanism, we set $T_c = \frac{T}{8}$ (unless otherwise specified), with T being the optical period. The classical model can help us understand different types of excitation-related channels [41]. Although the transition rate for various channels from the quantum model will carry additional information such as resonance enhancement, the key point that we want to study is the characteristics of different channels; resonance enhancement will influence the transition rate of the resonance channel but may not play an important role in the characteristics of correlated momentum spectra for the various channels. Thus, the resonance effect is unimportant in most cases and we can study the channel-resolved correlated momentum spectra quantitatively based on the CTMC model [7,8,10,11].

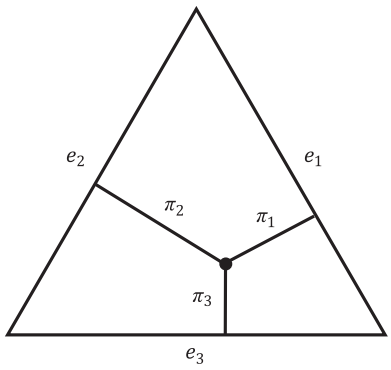

FIG. 1. Sketch of a Dalitz plot. The correlated momenta of three electrons are mapped onto points in the triangle. The coordinates of these points are determined by (π_1, π_2, π_3), where π_i indicates the distance from the point to the ith border.

The final momenta of TI events are mapped onto the Dalitz plot [12] sketched in Fig. 1. We focus on the momentum along the laser polarization direction. In Fig. 1 we define the coordinates of the point in the spectrum as

$$\pi_i = \left|\frac{p_{i,x}}{\sqrt{p_{1,x}^2 + p_{2,x}^2 + p_{3,x}^2}}\right|^2, \quad i = 1, 2, 3, \quad (7)$$

where π_i may indicate the distances to the ith border of the triangle. Here $p_{i,x}$ is the momentum of the ith electron along the laser polarization direction. To include the information on momentum directions which are not contained in Fig. 1, one may collect events in the representations indicated by (ppp) or (ppm), where p and m denote the directions parallel and antiparallel to the x axis, respectively (which exactly correspond to the $+$ and $-$ notation introduced in [12]). Since the three electrons are physically identical and cannot be distinguished, the symmetrical treatment for three electrons is performed in simulations. However, the electrons are distinguishable in the classical model, which makes it possible to extract information by tracing the trajectory for a particular electron. In simulations, we use a multicycle laser pulse, and thus the effects induced by the carrier envelope phase are negligible. One may expect that the spectra in (ppp) and (mmm) representations are the same. A similar conclusion holds for representations (ppm) and (pmm) when three electrons are undistinguished, of which we consider the first one only.

In total, more than 10^9 trajectories are calculated and more than 10^5 TI events are collected to obtain converged results. In practical cases when the laser intensity is extremely weak, the TI rate is so low (lower than 10^{-5}) that it is necessary to calculate more than 10^{10} trajectories.

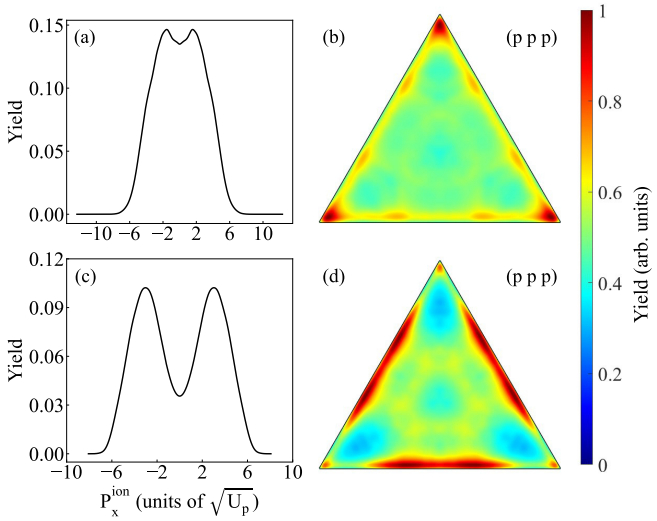

FIG. 2. (a) and (c) Ion momentum distribution for Ne^{3+}. (b) and (d) Ternary spectra with symmetrical treatment in the (*ppp*) representation. The pictures are normalized. The intensities of the seven-cycle 800-nm laser pulses are (a) and (b) 3.0×10^{14} W/cm^2 and (c) and (d) 7.0×10^{14} W/cm^2.

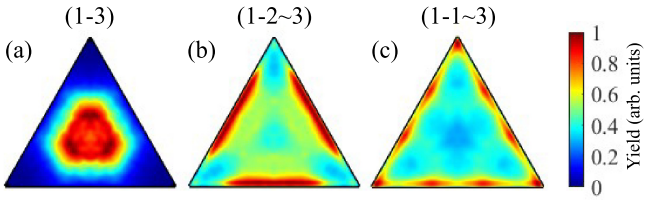

FIG. 3. Ternary spectra with symmetrical treatment in the (*ppp*) representation for different NSTI channels: (a) channel (1-3), (b) channel (1-2∼3), and (c) channel (1-1∼3). The laser intensity is 7.0×10^{14} W/cm^2 and the laser wavelength is 800 nm.

III. RESULTS AND DISCUSSION

A. Dalitz plots in the (*ppp*) representation

In this section we study the NSTI of Ne under 800-nm laser fields in the (*ppp*) representation. The laser intensities are below 8.0×10^{14} W/cm^2. Previous experimental and theoretical works [21,39,40] implied that for these laser parameters the recollision occurs once in the three-electron release. For clarity, we follow the definition of the various triple ionization channels proposed in Ref. [41] and only briefly reference it here. The channels involving a single recollision event are (1-3), (1-2∼3), and (1-1∼3). Here - denotes recollision while ∼ stands for emission without recollision, and numbers indicate the number of free electrons at that moment. In the channel (1-3), the tunneling electron e_3 returns to collide with the two bound electrons e_1 and e_2 and three electrons are emitted immediately within $\frac{T}{8}$ after the recollision. It is clear that this channel represents the direct $(e, 3e)$ process. In the channel (1-2∼3), after the rescattering of e_3, only two electrons (any two of the three electrons) are emitted within $\frac{T}{8}$; the remaining electron is excited and will be released when the next wave crest comes. Such a description meets the definition of the RESI process [51,52]. In the channel (1-1∼3), only one electron (any one of the three electrons) is emitted within $\frac{T}{8}$ after the rescattering of e_3 and the two remaining electrons are released via RESI afterward.

In Fig. 2 we compare the ternary spectrum with the ion momentum distribution for two laser intensities. From Figs. 2(a) and 2(c) one can see that the double-hump structure becomes more pronounced when the laser intensity increases from 3.0×10^{14} W/cm^2 to 7.0×10^{14} W/cm^2. However, since all possible triple-ionization channels contribute to the ion momentum distribution [39–41], it is unclear, without additional simulations, which of them are present or in what proportion they contribute. The situation is quite different in the case of ternary spectra [see Figs. 2(b) and 2(d)]. Distinct areas of the triangles are filled for different laser intensities. It turns out that these areas can be associated with different triple-ionization channels. In this way, the analysis of the real experimental spectra will allow the identification of the dominant ionization channel under the given conditions.

To determine which regions of the ternary spectrum are populated by which of the trajectories, in Fig. 3 we show three separate ternary spectra obtained from trajectories assigned to the main one-recollision channels (1-3), (1-2∼3), and (1-1∼3), respectively. In the channel (1-3) [see Fig. 3(a)], all electrons are released simultaneously, so they acquire similar drift momenta in the laser field, i.e., three electrons all have similar energies; therefore, the distribution is located around the center of the triangle and has trifold symmetry. In the channel (1-2∼3) [see Fig. 3(b)], one of the electrons is freed via the RESI mechanism and consequently gains a little drift momentum. However, the first two electrons are emitted simultaneously soon after the recollision that happens around the zero of the electric field. Because the drift momentum is determined by the vector potential at the recollision time, these two electrons end up with relatively high and similar momenta. As a result, the distribution of the channel (1-2∼3) in the ternary spectrum is located close to the borders and is symmetrical about the midpoint of the edge. Finally, in the channel (1-1∼3) [see Fig. 3(c)], two electrons are released close to the maxima of the laser field and they tend to pick up a little drift momentum; thus the main distribution is close to the corners of the triangle. Some additional distributions are present on the edge close to the midpoint (we discuss their origin below).

To infer how the features observed on the ternary spectra of each ionization channel are formed, we take advantage of the classicality of the simulation method we use and analyze the data without the symmetrical treatment (see Fig. 4). The electron-resolved spectrum for the events from the channel (1-3) is shown in Fig. 4(a). Due to the lack of symmetrical treatment, the causality in the time domain is easy to trace, i.e., e_3 is the electron that tunnels first and e_1 and e_2 are the two initially bound electrons. The whole distribution is close to the e_3 edge, which means that e_3 tends to have a lower momentum than the other two electrons. There are two types of maxima visible in the distribution: Type-I is located exactly on the altitude falling from the corner corresponding to electron e_3 (solid circle) and type-II is located symmetrically with respect to that altitude (dotted circles). For the events contributing to the type-I maximum, e_3 has the lowest momentum of the

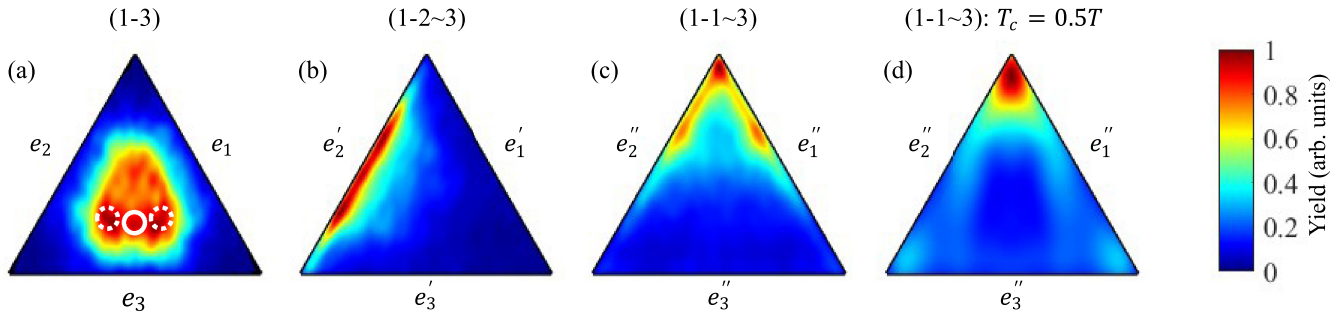

FIG. 4. Electron-resolved ternary spectra for different channels in the (ppp) representation. The channels in different panels are marked above the panels. The dotted and solid circles in (a) represent two types of dynamics, respectively. The laser intensity is 7.0×10^{14} W/cm^2 and the laser wavelength is 800 nm.

three electrons, while e_1 and e_2 carry similar higher momenta. The events that make up the type-II maximum have a hierarchy of momentum sharing, i.e., either e_1 carries the highest momentum among three electrons or e_2 carries the highest momentum. The other two electrons both have lower but similar momenta. In both types, the energy is shared asymmetrically between three electrons. When the laser intensity is 7.0×10^{14} W/cm^2, the corresponding $3.17U_p$ equals 4.86 a.u. (higher than the $I_{p2} + I_{p3}$ of Ne). Hence, the maximum rescattering energy is high enough to kick off two bound electrons together with certain residual energy. The dynamics behind the type-I maximum may be qualitatively described in the following way: e_3 is slowed down on return because of the interaction with the two bound electrons. The bound electrons acquire enough energy to be emitted and are then accelerated by the laser field, while e_3 still has residual momentum with an opposite direction as compared to the laser electric field force and will continue to slow down, which results in a low final momentum for it. The following is the sequence of events behind the type-II maximum: e_3 returns with high momentum and during recollision kicks out one of the bound electrons that has an initial momentum of opposite direction with respect to the laser electric field force. These two electrons will be slowed down by the field; thus they end up with lower final momenta as compared to the other bound electron. Note that the latter electron is emitted immediately after the recollision and is accelerated by the laser field. Under the laser intensity considered, the probability of type-II is higher [see Fig. 4(a)]. The described dynamics is similar to that responsible for the fingerlike structures observed in double ionization [7,8].

In Fig. 4(b) we present events corresponding to the channel (1-2~3). Here the freed electrons right after the recollision are e_1' and e_3'. They tend to have high momenta and the third electron (it is e_2' in the depicted case) carries very little momentum. Therefore, the distribution is located along the e_2' border, close to its midpoint. In Fig. 4(c) we present events corresponding to the channel (1-1~3), in which e_3'' is the only electron emitted within $\frac{T}{8}$ after the rescattering and it carries a high drift momentum; thus the distribution is located in the upper region of the triangle. The remaining two electrons are released by the laser field at later times. If one of the remaining electrons is pumped into a highly excited state, it might be emitted within $\frac{T}{4}$ with a momentum that is a bit lower than that carried by e_3'' but much higher than that carried by the last emitted electron. Such a sequence of events is the reason why the signal is seen in the upper half of the borders in Fig. 4(c). In Fig. 4(d) we collect the events in the channel (1-1~3) that have a time difference between the emission of e_1'' (or e_2'') and the rescattering larger than $0.5T$ ($T_c = 0.5T$), which corresponds to selecting cases with both electrons being emitted close to the field maximum (without highly excited states). Such a pick results in the distribution shrunken to the corner.

Based on the above analysis, the ternary spectrum in the (ppp) representation may be divided into three regions, each of which corresponds to one of the three main channels with a single recollision event (see Fig. 5). Then we can extract the ionization channels as well as their relative proportions from the spectra similar to those presented in Fig. 2. For the data presented in Fig. 2(b), the channel (1-1~3) dominates. However, when the laser intensity increases [see Fig. 2(d)], the role of the channel (1-2~3) grows and a weak indication of the presence of the channel (1-3) appears. The scheme presented in Fig. 5 can help to directly extract the ionization mechanisms when the intensity of the laser is not very high (i.e., when channels with single recollision dominate NSTI). The presented method of interpretation of the ternary spectra in the (ppp) representation is important for both experiment and theory. In particular, in the latter case, one may obtain the ternary spectrum through the TDSE simulations [12] though the information of ionization channels is hard to extract directly solely from quantum simulations. However, with the help of Fig. 5, one can immediately analyze the mechanisms

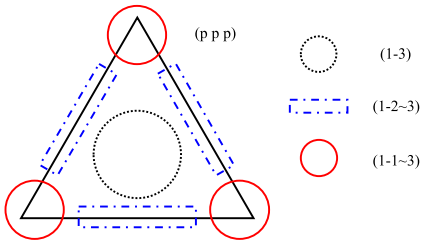

FIG. 5. Demonstration of how to extract NSTI channels through the ternary spectrum in the (ppp) representation.

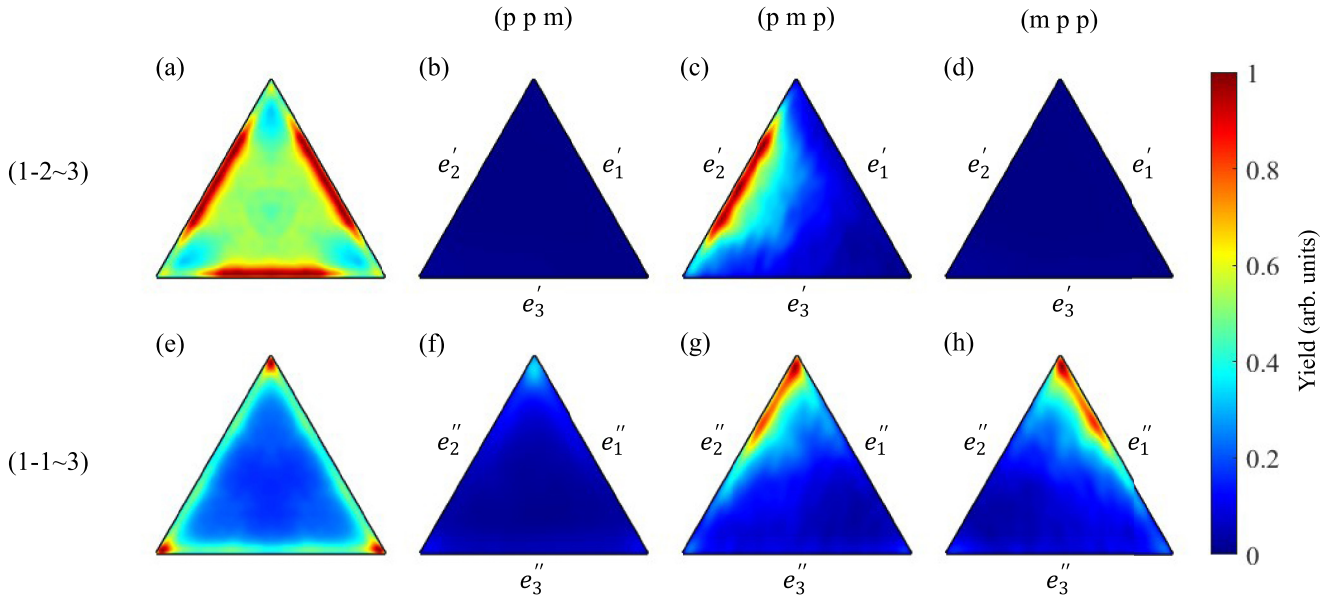

FIG. 6. (a) and (e) Ternary spectra with symmetrical treatment for the channels (a) (1-2∼3) and (e) (1-1∼3) in the (*ppm*) representation. (b)–(d) Ternary spectra without symmetrical treatment for the channel (1-2∼3). (f)–(h) Ternary spectra without symmetrical treatment for the channel (1-1∼3). The representations at the top mean the directions of e_1', e_2', and e_3' (e_1'', e_2'', and e_3''), respectively. The electron notation is the same as that used in Fig. 4. The spectra in (a) and (e) are normalized by their own maxima. (b)–(d) and (f)–(h) share the same color bar, respectively. The laser intensity is 7.0×10^{14} W/cm^2 and the laser wavelength is 800 nm.

of ionization, as long as the information on correlated momenta of the three electrons is available.

B. Dalitz plots in the (*ppm*) representation

In this section we study the NSTI channels of Ne in the (*ppm*) representation, i.e., one electron has momentum in the opposite direction compared to the momentum directions of the other two electrons. In Figs. 6(a) and 6(e) we present the spectra with symmetrical treatment for the channels (1-2∼3) and (1-1∼3), respectively. To analyze the details of dynamics, we examine relevant spectra without the symmetrical treatment [see Figs. 6(b)–6(d) and 6(f)–6(h)]. All electrons from the channel (1-3) have the same momentum direction; hence there is no corresponding distribution in the (*ppm*) representation.

We start with an analysis of the ternary spectra with symmetrical treatment. In the channel (1-2∼3), the two electrons emitted simultaneously after the recollision have high momenta with the same direction and the remaining electron emitted by RESI carries a low drift momentum with the opposite direction. The distribution in Fig. 6(a) resembles the result presented in Fig. 3(b). In the channel (1-1∼3), the first emitted electron carries a high momentum while the other two electrons are freed by RESI with the opposite direction; thus the distribution shown in Fig. 6(e) resembles the one shown in Fig. 3(c).

The electron-resolved ternary spectra in the (*ppm*) representation are more complex than those in the (*ppp*) representation. In Figs. 6(b)–6(d) and 6(f)–6(h) we show such spectra for the channels (1-2∼3) and (1-1∼3), respectively. Because one of the electrons has the opposite momentum direction (it can be any one of the three electrons), we need to consider three different representations for each channel. In Figs. 6(b) and 6(f), e_3' and e_3'', respectively, have the opposite momentum direction as compared to the other two electrons. In Figs. 6(c) and 6(g) the electrons with the opposite momentum direction are e_2' and e_2'' and in Figs. 6(d) and 6(h) e_1' and e_1'', respectively. The notation for electrons used in Fig. 6 is the same as that in Fig. 4. In the channel (1-2∼3), e_1' and e_3' must have the same direction (they are emitted together within $\frac{T}{8}$); therefore, in Figs. 6(b) and 6(d) there is no signal and all are registered in Fig. 6(c). In the channel (1-1∼3), however [Fig. 6(f)], there is a very weak signal in the e_3'' corner because e_1'' and e_2'' are both released around the maximum of the laser field and they end up with low momentum pointing in the same direction. Such a scenario happens much less frequently than those responsible for the distributions in Figs. 6(g) and 6(h). This is because one of the bounded electrons tends to be sent into a highly excited state during the recollision. If e_1'' is sent to a highly excited state, then it will be emitted in the same direction as e_3'' within a smaller time delay. Because the recollision time is around the zero of the laser field, e_3'' tends to have the highest drift momentum. Thus, the momentum of e_1'' will usually be lower than that of e_3''. This situation corresponds to Fig. 6(g). When e_2'' is sent to a highly excited state, the situation corresponds to Fig. 6(h) and the dynamics is similar to that responsible for distribution in Fig. 6(g).

Based on the above analysis, the ternary spectrum in the (*ppm*) representation may be divided into two regions corresponding to the channels (1-2∼3) and (1-1∼3), as depicted in Fig. 7. A natural question therefore arises as to whether there exist a channel that is represented by a distribution mainly located around the center of the ternary spectrum in the (*ppm*) representation. When the analysis is restricted to trajectories with a single-recollision event, the answer is negative. Indeed,

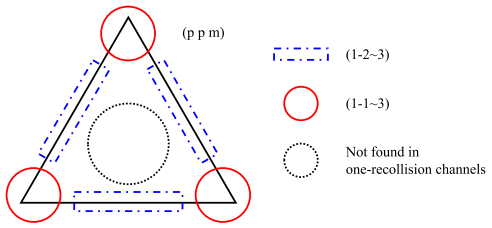

FIG. 7. Demonstration of how to extract NSTI channels through the ternary spectrum in the (ppm) representation.

for the laser intensities under which the one-recollision nonsequential ionization dominates, the signals of the spectra are always located around the border due to the participation of RESI. Hence, to observe the distribution around the center in the (ppm) representation, the dominant ionization channel should not contain the RESI mechanism. Additionally, three electrons should not be emitted within the same half laser cycle. To satisfy the above conditions, multiple-recollision channels have to be taken into account. The special properties of the ternary spectra of multirecollision channels will be analyzed in the following section.

C. Multirecollision regime

The ion momentum distribution of multirecollision channel has been partly studied in previous work [41]. The recollisions tend to happen around the zeros of the laser field, i.e., the time difference between recollisions is approximately equal to multiples of $\frac{T}{2}$. If the time difference between the two recollisions approximately equals multiples of T, three electrons will have similar drift momenta, in terms of both direction and value, and the final ternary spectrum in the (ppp) representation will show a maximum value around the center (temporarily ignore the influence of RESI). However, the ternary spectrum in the (ppp) representation does not allow one to differentiate between the channel (1-3) and multirecollision channels; therefore, we focus on the (ppm) representation further in this section. If the time difference between two recollisions approximately equals $(2n+1)\frac{T}{2}$ $(n = 1, 2, 3, \ldots)$, then the drift momenta of the two electrons emitted later will have the opposite direction (the absolute values are close) as compared to the electron emitted first. Consequently, the final ternary spectrum in the (ppm) representation will show a maximum value around the center. If one considers the ion momentum only, the discussed ionization channel will be mixed with other channels, while in the ternary spectrum under the (ppm) representation, it is clearly separated provided the RESI mechanism is strongly suppressed. There are two main difficulties in observing the multirecollision channel without RESI: (i) The proportion of the multirecollision events among all TIs is usually very small [41] and (ii) it is difficult to simultaneously enhance multirecollision events and suppress RESI events. In this section we find ways to surmount these two problems.

Let us investigate a typical case of the multirecollision channel in its time evolution, i.e., the energy of each electron as a function of time, as shown in Fig. 8(a). The laser parameters are set so that the ponderomotive energy is 0.3946 a.u. In this channel, only one electron (can be any of the three

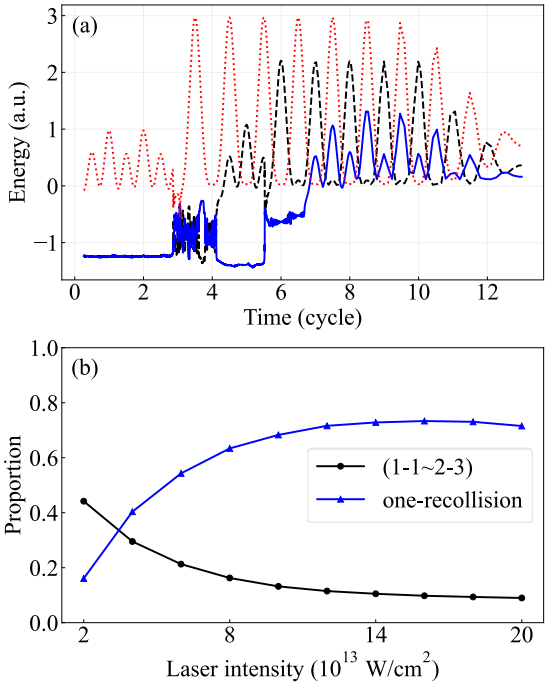

FIG. 8. (a) Time evolution of electron energies for the channel (1-1∼2-3) of Ar. The black dashed, blue solid, and red dotted lines are for e_1, e_2, and e_3, respectively. The laser intensity is 2.0×10^{13} W/cm^2. The laser wavelength is 2400 nm. (b) Proportions of the channel (1-1∼2-3) and the one-recollision channels [sum of the channels (1-3), (1-2∼3), and (1-1∼3)] under different laser intensities for Ar. The ponderomotive energy of the laser field is fixed at 0.3946 a.u.

electrons) is emitted within $\frac{T}{2}$ after the first rescattering of e_3; the remaining two electrons are both excited and undergo interaction for some time. Then, at an instant approximately equal to $4T$ [see Fig. 8(a)], one of the bound electrons is dumped and kicks out the other bound electron. The freed electron returns at approximately $5.5T$ and recollides with the remaining electron. Because $3.17U_p$ in this laser field parameters is 1.25 a.u., which is lower than the third ionization potential of Ar (1.5 a.u.), the last electron is released by the RESI mechanism. We label this channel a mixed channel (1-1∼2-3), in which double excitation is followed by NSDI (via RESI). To study the importance of that channel we check its proportion in comparison to the proportions of all one-recollision channels, counted together, as the laser intensity increases while the ponderomotive energy is kept constant ($3.17U_p = 1.25$ a.u.) [see Fig. 8(b)]. Only for the lowest intensities, the channel (1-1∼2-3) dominates the other channels. When the laser intensity is 2.0×10^{13} W/cm^2, nearly half of the TI events belong to the channel (1-1∼2-3); there is only a small proportion of the one-recollision events and the rest of the cases belong to other types of multirecollision channels. Thus, keeping $3.17U_p$ close to the third ionization potential I_{p3} (1.5 a.u. for Ar) while reducing the laser intensity can enhance the proportion of the channel (1-1∼2-3) with respect to others. The purpose of keeping U_p at such a constant is just to suppress RESI. In principle, $3.17U_p$ should

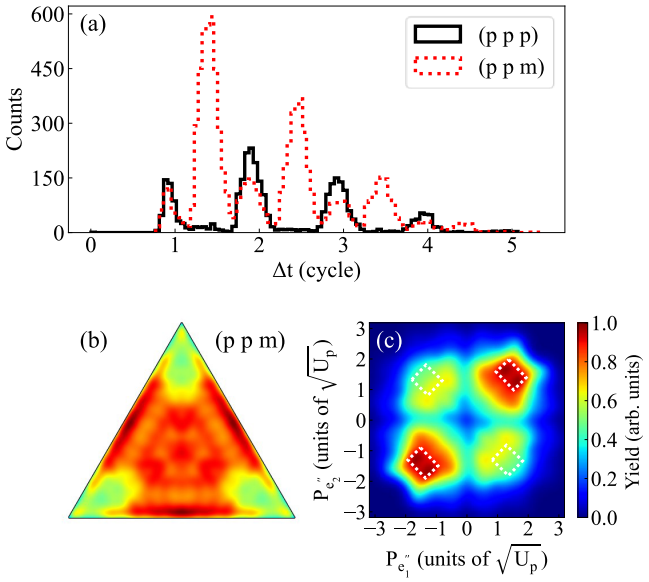

FIG. 9. (a) Distribution of the time difference between two recollisions in the channel (1-1∼2-3). The black solid line is for the events counted in the (*ppp*) representation and the red dotted line is for the events counted in the (*ppm*) representation. (b) Ternary spectrum of the channel (1-1∼2-3) in the (*ppm*) representation. The laser intensity is 2.0×10^{13} W/cm^2 and the laser wavelength is 2400 nm. (c) Correlated momentum spectrum of the two electrons that emit later by the second recollision. The target atom Ar has been used in the calculations in (a)–(c).

be a bit higher than I_{p3} to suppress RESI more successfully. However, if $3.17U_p = 1.5$ a.u., even for the laser intensity 2.0×10^{13} W/cm^2, the proportion of one-recollision channels will be larger than 30%. Further reduction of the laser intensity leads to an extremely low TI rate, i.e., lower than 10^{-6}, and it is difficult to perform reliable simulations. Also, we choose Ar as our target atom in this section instead of Ne (the bound energy of Ne is higher than that of Ar); thus we need a longer wavelength, leading to a lower TI rate. Based on the above analysis, we set the laser parameters to be 2400 nm and 2.0×10^{13} W/cm^2. Under these parameters, the channel (1-1∼2-3) dominates and its ternary spectrum will be discussed in the following.

As discussed above, the time difference between the successive recollisions is an appropriate parameter to determine whether all electrons will have the same momentum direction or not. Therefore, in Fig. 9(a) we show the distributions of the time difference between two recollisions for events from the channel (1-1∼2-3) counted in the (*ppp*) and (*ppm*) representations, respectively. Indeed, in the (*ppp*) representation, the distribution of the time difference has maxima at time instants around integer multiples of T. However, in the (*ppm*) representation, the distribution has maxima at all time instants being odd multiples of $\frac{T}{2}$. Such time differences between recollisions certainly lead to a situation where one of the electrons has the opposite momentum direction with respect to the other two. The distribution has also maxima at even multiples of $T/2$, though these peaks are much lower. This is due to the fact that $3.17U_p$ is a bit lower than I_{p3} and RESI is still possible, and thus the last electron may carry momentum with a different direction from the other two. Interestingly, the maxima at $1.5T$ and $2.5T$ in the (*ppm*) representation are both higher than the highest maximum in the (*ppp*) representation (the maximum at $1.5T$ is even three times higher). Taking into account that all peaks have comparable widths, this means that among all events in the channel (1-1∼2-3), the biggest proportion falls into the (*ppm*) representation. In Fig. 9(b) we show the ternary spectrum for the events from the channel (1-1∼2-3); it is very different from the ones we discussed when analyzing the one-recollision channel. The signal around the center can be understood with the help of the two-electron momentum distribution shown in Fig. 9(c). Here e_1'' and e_2'' are the two electrons that are emitted after the second recollision; the signals around the center of the ternary spectrum come from the regions which are framed by the dotted lines in Fig. 9(c). The signals present next to the borders of the ternary spectrum come from the regions which are close to the axes in the two-electron distribution (RESI induced). The fact that a considerable signal can be found at the center in the (*ppm*) representation shows the special property of multirecollision channels. In principle, if it were possible to lower the laser intensity further while setting the value of $3.17U_p$ slightly higher than I_{p3}, the RESI mechanism would be even more suppressed and a stronger signal would be seen around the center of the ternary spectrum. If this scenario could be implemented in experiments, even if it is not possible to measure distributions of correlated momenta for three electrons simultaneously now, it is still possible to extract information about the presence of multiple-recollision channels through the ion momentum distributions. The ion momentum distribution for events that contribute to distributions in the (*ppp*) representation has maxima around $3A_0$ (A_0 being the amplitude of the vector potential), while the ion momentum distribution for events that contribute to distributions in the (*ppm*) representation has maxima around A_0. Thus, four energy peaks in the ion momentum distribution might be expected.

IV. CONCLUSION

We performed channel-resolved semiclassical simulations for nonsequential channels of triple ionization of atoms, in particular Ar and Ne. We found that mapping the three-electron momenta onto the Dalitz plots allows for direct extraction of the NSTI channels. We defined the two representations that cover the possible combination of electronic motion directions. In the (*ppp*) representation, the three main channels characterized by one recollision [(1-3), (1-2∼3), and (1-1∼3)] can be made to correspond to the three different regions (center, border, and corner) on a Dalitz plot. The case of the (*ppm*) representation implies that the channels (1-2∼3) and (1-1∼3) fall onto the border and corner regions, respectively, while the normal one-recollision channels cannot show a maximum around the center of a ternary spectrum. However, a considerable signal around the center is noticeable for multirecollision channels. Such channels can be made dominant by decreasing the laser intensity while keeping the ponderomotive energy of the tunneled electron constant (between I_{p2} and I_{p3}).

We found that one can reveal manifestations of electron correlation by performing an analysis of electron-resolved ternary spectra. For the direct (1-3) channel there is an asymmetry energy sharing on Dalitz plots that resembles the effect behind the famous fingerlike pattern in NSDI. The structures corresponding to the multirecollision channels may be tricky to trace in experiment, as usually one cannot decrease the laser intensity as drastically as we did in our simulations because the ionization yield is too low for clear detection. However, one can possibly eliminate such a problem by using an additional XUV source for bursting the initial electron production and thus making the final three-electron signal strong enough for detection.

ACKNOWLEDGMENTS

This work was supported by National Natural Science Foundation of China (Grants No. 11925405 and No. 91850203) and National Science Centre (Poland) Symfonia Project No. 2016/20/W/ST4/00314. Simulations were performed on the π supercomputer at Shanghai Jiao Tong University.

[1] W. Becker, X. J. Liu, P. J. Ho, and J. H. Eberly, Rev. Mod. Phys. **84**, 1011 (2012).
[2] F. Krausz and M. Ivanov, Rev. Mod. Phys. **81**, 163 (2009).
[3] U. S. Sainadh, H. Xu, X. Wang, A. Atia-Tul-Noo, W. C. Wallace, N. Douguet, A. Bray, I. Ivanov, K. Bartschat, A. Kheifets, R. T. Sang, and I. V. Litvinyuk, Nature (London) **568**, 75 (2019).
[4] B. Walker, B. Sheehy, L. F. DiMauro, P. Agostini, K. J. Schafer, and K. C. Kulander, Phys. Rev. Lett. **73**, 1227 (1994).
[5] S. Augst, A. Talebpour, S. L. Chin, Y. Beaudoin, and M. Chaker, Phys. Rev. A **52**, R917 (1995).
[6] T. Weber, H. Giessen, M. Weckenbrock, G. Urbasch, A. Staudte, L. Spielberger, O. Jagutzki, V. Mergel, M. Vollmer, and R. Dörner, Nature (London) **405**, 658 (2000).
[7] A. Rudenko, V. L. B. de Jesus, T. Ergler, K. Zrost, B. Feuerstein, C. D. Schröter, R. Moshammer, and J. Ullrich, Phys. Rev. Lett. **99**, 263003 (2007).
[8] D. F. Ye, X. Liu, and J. Liu, Phys. Rev. Lett. **101**, 233003 (2008).
[9] B. Bergues, M. Kübel, N. G. Johnson, B. Fischer, N. Camus, K. J. Betsch, O. Herrwerth, A. Senftleben, A. M. Sayler, T. Rathje, T. Pfeifer, I. Ben-Itzhak, R. R. Jones, G. G. Paulus, F. Krausz, R. Moshammer, J. Ullrich, and M. F. Kling, Nat. Commun. **3**, 813 (2012).
[10] X. Sun, M. Li, D. Ye, G. Xin, L. Fu, X. Xie, Y. Deng, C. Wu, J. Liu, Q. Gong, and Y. Liu, Phys. Rev. Lett. **113**, 103001 (2014).
[11] G. P. Katsoulis, A. Hadjipittas, B. Bergues, M. F. Kling, and A. Emmanouilidou, Phys. Rev. Lett. **121**, 263203 (2018).
[12] D. K. Efimov, A. Maksymov, M. Ciappina, J. S. Prauzner-Bechcicki, M. Lewenstein, and J. Zakrzewski, Opt. Express **29**, 26526 (2021).
[13] G. Basnayake, S. Fernando, S. K. Lee, D. A. Debrah, G. A. Stewart, and W. Li, Molecular Physics **120**, e1931722 (2021).
[14] C. Figueira de Morisson Faria and X. Liu, J. Mod. Opt. **58**, 1076 (2011).
[15] S. Pabst and R. Santra, Phys. Rev. Lett. **111**, 233005 (2013).
[16] A. W. Bray, D. Freeman, S. Eckart, and A. S. Kheifets, Phys. Rev. A **100**, 013404 (2019).
[17] J. H. Thiede, B. Eckhardt, D. K. Efimov, J. S. Prauzner-Bechcicki, and J. Zakrzewski, Phys. Rev. A **98**, 031401(R) (2018).
[18] M. Schulz, R. Moshammer, W. Schmitt, H. Kollmus, R. Mann, S. Hagmann, R. E. Olson, and J. Ullrich, Phys. Rev. A **61**, 022703 (2000).
[19] A. Rudenko, K. Zrost, B. Feuerstein, V. L. B. de Jesus, C. D. Schröter, R. Moshammer, and J. Ullrich, Phys. Rev. Lett. **93**, 253001 (2004).
[20] K. Zrost, A. Rudenko, T. Ergler, B. Feuerstein, V. L. B. de Jesus, C. D. Schröter, R. Moshammer, and J. Ullrich, J. Phys. B **39**, S371 (2006).
[21] A. Rudenko, T. Ergler, K. Zrost, B. Feuerstein, V. L. B. de Jesus, C. D. Schröter, R. Moshammer, and J. Ullrich, J. Phys. B **41**, 081006 (2008).
[22] O. Herrwerth, A. Rudenko, M. Kremer, V. L. B. de Jesus, B. Fischer, G. Gademann, K. Simeonidis, A. Achtelik, T. Ergler, B. Feuerstein, C. D. Schröter, R. Moshammer, and J. Ullrich, New J. Phys. **10**, 025007 (2008).
[23] S. Zhong, J. Vinbladh, D. Busto, R. J. Squibb, M. Isinger, L. Neoričić, H. Laurell, R. Weissenbilder, C. L. Arnold, R. Feifel, J. M. Dahlström, G. Wendin, M. Gisselbrecht, E. Lindroth, and A. L'Huillier, Nat. Commun. **11**, 5042 (2020).
[24] S. Mikaelsson, J. Vogelsang, C. Guo, I. Sytcevich, A.-L. Viotti, F. Langer, Y.-C. Cheng, S. Nandi, W. Jin, A. Olofsson, R. Weissenbilder, J. Mauritsson, A. L'Huillier, M. Gisselbrecht, and C. L. Arnold, Nanophotonics **10**, 117 (2020).
[25] K. Amini, J. Biegert, F. Calegari, A. Chacón, M. F. Ciappina, A. Dauphin, D. K. Efimov, C. Figueira de Morisson Faria, K. Giergiel, P. Gniewek, A. S. Landsman, M. Lesiuk, M. Mandrysz, A. S. Maxwell, R. Moszyński, L. Ortmann, J. A. Pérez-Hernández, A. Picón, E. Pisanty, J. Prauzner-Bechcicki, *et al.*, Rep. Prog. Phys. **82**, 116001 (2019).
[26] J. Colgan, M. S. Pindzola, and F. Robicheaux, Phys. Rev. Lett. **93**, 053201 (2004).
[27] J. Colgan, A. Emmanouilidou, and M. S. Pindzola, Phys. Rev. Lett. **110**, 063001 (2013).
[28] C. Ruiz, L. Plaja, and L. Roso, Phys. Rev. Lett. **94**, 063002 (2005).
[29] J. S. Prauzner-Bechcicki, K. Sacha, B. Eckhardt, and J. Zakrzewski, Phys. Rev. Lett. **98**, 203002 (2007).
[30] J. S. Prauzner-Bechcicki, K. Sacha, B. Eckhardt, and J. Zakrzewski, Phys. Rev. A **78**, 013419 (2008).
[31] D. K. Efimov, J. S. Prauzner-Bechcicki, J. H. Thiede, B. Eckhardt, and J. Zakrzewski, Phys. Rev. A **100**, 063408 (2019).
[32] D. K. Efimov, J. S. Prauzner-Bechcicki, and J. Zakrzewski, Phys. Rev. A **101**, 063402 (2020).
[33] J. S. Prauzner-Bechcicki, D. K. Efimov, M. Mandrysz, and J. Zakrzewski, J. Phys. B **54**, 114001 (2021).
[34] A. M. Sayler, J. McKenna, B. Gaire, N. G. Kling, K. D. Carnes, and I. Ben-Itzhak, Phys. Rev. A **86**, 033425 (2012).

[35] K. Sacha and B. Eckhardt, Phys. Rev. A **64**, 053401 (2001).
[36] P. J. Ho and J. H. Eberly, Phys. Rev. Lett. **97**, 083001 (2006).
[37] P. J. Ho and J. H. Eberly, Opt. Express **15**, 1845 (2007).
[38] J. Guo and X.-S. Liu, Phys. Rev. A **78**, 013401 (2008).
[39] Y. Zhou, Q. Liao, and P. Lu, Opt. Express **18**, 16025 (2010).
[40] Q. Tang, C. Huang, Y. Zhou, and P. Lu, Opt. Express **21**, 21433 (2013).
[41] H. Jiang and F. He, Phys. Rev. A **104**, 023113 (2021).
[42] M. B. Peters, V. P. Majety, and A. Emmanouilidou, Phys. Rev. A **103**, 043109 (2021).
[43] Z.-Q. Yuan, D.-F. Ye, Y.-Q. Gu, J. Liu, and L.-B. Fu, Opt. Express **27**, 3180 (2019).
[44] N. B. Delone and V. P. Krainov, J. Opt. Soc. Am. B **8**, 1207 (1991).
[45] C. L. Kirschbaum and L. Wilets, Phys. Rev. A **21**, 834 (1980).
[46] J. S. Cohen, Phys. Rev. A **51**, 266 (1995).
[47] J. S. Cohen, Phys. Rev. A **54**, 573 (1996).
[48] Y. M. Zhou, C. Huang, Q. Liao, and P. X. Lu, Phys. Rev. Lett. **109**, 053004 (2012).
[49] S. Liu, D. Ye, and J. Liu, J. Phys. B **53**, 145005 (2020).
[50] J. C. Baggesen and L. B. Madsen, Phys. Rev. Lett. **104**, 043602 (2010).
[51] B. Feuerstein, R. Moshammer, D. Fischer, A. Dorn, C. D. Schröter, J. Deipenwisch, J. R. Crespo Lopez-Urrutia, C. Höhr, P. Neumayer, J. Ullrich, H. Rottke, C. Trump, M. Wittmann, G. Korn, and W. Sandner, Phys. Rev. Lett. **87**, 043003 (2001).
[52] V. L. B. de Jesus, B. Feuerstein, K. Zrost, D. Fischer, A. Rudenko, F. Afaneh, C. D. Schröter, R. Moshammer, and J. Ullrich, J. Phys. B **37**, L161 (2004).